

Radio, optical and infrared observations of CLASS B0128+437

A. D. Biggs,^{1,2*} I. W. A. Browne,² N. J. Jackson,² T. York,² M. A. Norbury,²
J. P. McKean² and P. M. Phillips²

¹Joint Institute for VLBI in Europe, Postbus 2, 7990 AA Dwingeloo, the Netherlands

²University of Manchester, Jodrell Bank Observatory, Macclesfield, Cheshire SK11 9DL

Accepted 2004 February 4. Received 2004 January 16; in original form 2003 June 3

ABSTRACT

We present new observations of the gravitational lens system CLASS B0128+437 made in the optical, infrared and radio regimes. *Hubble Space Telescope* observations detect only a very faint, extended object in the *I* band with no obvious emission from the lensed images visible; no detection at all is made in the *V* band. The lens system is detected with a much higher signal-to-noise ratio with the United Kingdom Infrared Telescope in the *K* band and, although resolved, the resolution is not sufficient to allow the lensed images and the lens galaxy to be separated. A careful astrometric calibration, however, suggests that the peak of the infrared emission corresponds to the two merging images A and B and therefore that the lensed images dominate at infrared wavelengths. The new radio data consist of high-resolution very long baseline interferometry radio images at three frequencies, 2.3, 5 and 8.4 GHz, made with the Very Long Baseline Array (VLBA) and the 100-m Effelsberg telescope. These reveal that the lensed source consists of three well-defined subcomponents that are embedded in a more extended jet. Due to the fact that the subcomponents have different spectral indices, it is possible to determine, unambiguously, which part of each image corresponds to the same source subcomponent. Our main finding is that one of the images, B, looks very different to the others, there being no obvious division into separate subcomponents and the image being apparently both broader and smoother. This is a consequence, we believe, of scatter-broadening in the interstellar medium of the lensing galaxy. The large number of multiply imaged source subcomponents also provides an abundance of modelling constraints and we have attempted to fit a singular isothermal ellipsoid + external shear model to the data, as well as utilizing the novel method of Evans and Witt. It proves difficult in both cases, however, to obtain a satisfactory fit, which strongly suggests the presence of substructure in the mass distribution of the lensing galaxy, perhaps of the kind that is predicted by cold dark matter theories of structure formation.

Key words: gravitational lensing – galaxies: ISM – quasars: individual: B0128+437.

1 INTRODUCTION

The Cosmic Lens All-Sky Survey (CLASS), a radio survey of the northern sky, has been exceptionally successful in discovering new arcsec-scale gravitational lens systems, with a final tally of 22 (Browne et al. 2003; Myers et al. 2003). Using the method of Refsdal (1964), these systems can be used individually to determine the Hubble parameter (e.g. Burud et al. 2002; Fassnacht et al. 2002; Treu & Koopmans 2002; Kochanek 2003) and together to place constraints on the cosmological parameters Ω_0 and λ_0 (e.g. Helbig et al. 1999; Chae et al. 2002). As well as this, gravitational

lenses are used to explore various aspects of high-redshift galaxies, i.e. the lens galaxies themselves (e.g. Kochanek et al. 2000; Lehár et al. 2000), including their distribution of ionized and magnetized plasma, their radial mass profiles (e.g. Muñoz, Kochanek & Keeton 2001; Rusin & Ma 2001; Rusin et al. 2002; Biggs et al. 2003; Koopmans & Treu 2003; Winn, Rusin & Kochanek 2003b) and the presence of massive substructures such as those predicted by cold dark matter (CDM) theories of large-scale structure formation (e.g. Mao & Schneider 1998; Metcalf & Madau 2001; Bradač et al. 2002; Dalal & Kochanek 2002; Metcalf 2002; Metcalf & Zhao 2002).

B0128+437 (Phillips et al. 2000) was discovered by CLASS and consists of four images with a maximum separation of 540 mas (Fig. 1). Initial modelling, in the absence of any information regarding the lensing galaxy, demonstrated that a singular isothermal

*E-mail: biggs@jive.nl

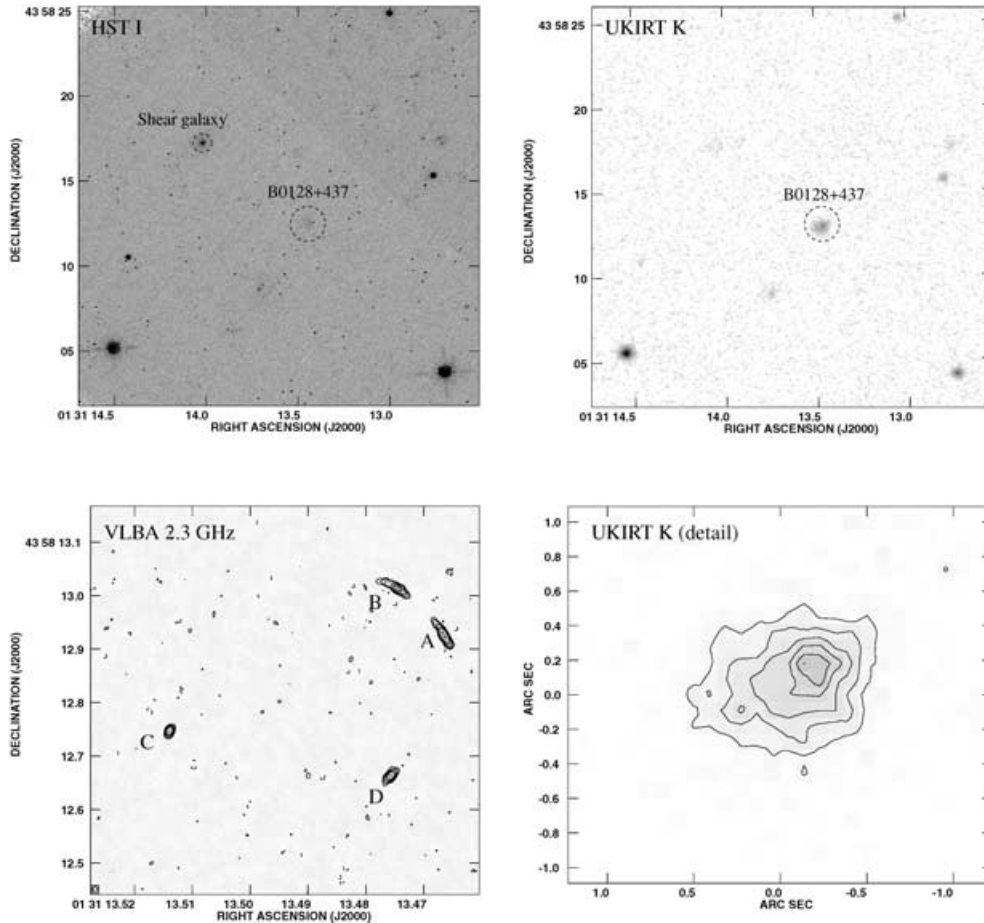


Figure 1. Top left: *HST* *I*-band image with both B0128+437 and the possible shear galaxy circled. The axes are labelled according to the original *HST* astrometric information. Top right: UKIRT *K*-band (2.2- μm) image with the astrometry calibrated as described in the text. The field of view in both images has been restricted to 23.5×23.5 arcsec² and each has been aligned using the positions of the two bright stars in the lower half of the frame. Bottom left: VLBA 2.3-GHz map (tapered) of B0128+437 that illustrates the image configuration. Bottom right: Contoured close-up of the UKIRT B0128+437 image illustrating the similarity between the radio and infrared structure.

ellipsoidal mass distribution plus a large external shear produces a good fit to the observed image positions and flux ratios. Subsequent optical spectroscopy with the W. M. Keck telescope (McKean et al. 2004) measured a redshift for the lensed source of $z_s = 3.12$ and identified a single line at a different redshift that is presumably that of the lensing galaxy. The most likely identification of this line ([O II]) gives a lens redshift of $z_d = 1.145$, although additional observations will be required to confirm this. The radio spectrum of the lensed source has a pronounced peak at around 1 GHz, thus making it a member of the gigahertz peaked spectrum (GPS) class.

In this paper we present new optical, infrared and radio very long baseline interferometry (VLBI) observations of B0128+437 which demonstrate that this system is far more interesting than the original 5-GHz multi-element radio-linked interferometer network (MERLIN) data suggested. In the next section we show images made using the *Hubble Space Telescope* (*HST*) and the United Kingdom Infrared Telescope (UKIRT). We then go on to describe new multifrequency observations (2.3, 5 and 8.4 GHz) made with the Very Long Baseline Array (VLBA) together with the 100-m Effelsberg telescope and we present the resulting maps of each of the lensed images. The remainder of the paper seeks to explain the strange appearance of image B and the difficulties found in fitting a lens model to the observed VLBI substructure.

2 OPTICAL AND INFRARED IMAGES

B0128+437 was observed with the *HST* on 2001 June 16 using the Wide Field and Planetary Camera 2 (WFPC2) giving a spatial sampling of $46 \text{ mas pixel}^{-1}$ at the location of the lens. Data were taken in both the F555W and F814W filters which correspond approximately to the standard Johnson–Cousins *V* and *I* bands, respectively. Four exposures were taken in each filter (a two-point dither pattern was used with two exposures taken at each pointing to enable cosmic ray removal) resulting in a total exposure time of 5400 s. The final images, produced using the Image Reduction and Analysis Facility (IRAF), show only a very faint and extended detection in the *I* band ($I = 23.8 \pm 0.2 \text{ mag}$) and none at all in the *V* band ($V > 25$). We show the *I*-band image in Fig. 1. There is no evidence of any light from the lensed images and so what light is detected probably originates in the lensing galaxy. However, the observations do identify a candidate shear galaxy 7.8 arcsec from B0128+437 at a position angle of 53° (consistent with the position angle found from the lens modelling of the MERLIN data) with a total flux of $24.2 \pm 0.4 \text{ mag}$ in *V* and $21.8 \pm 0.1 \text{ mag}$ in *I*.

An image with much higher signal-to-noise has been obtained with the UKIRT in the *K* band (2.2 μm). These observations were taken on 2000 September 5 using the UKIRT Fast Track Imager

(UFTI) which has a plate scale of $91 \text{ mas pixel}^{-1}$ and a field of view of 93 arcsec . A standard set of nine 60-s exposures were taken with the telescope offset by 10 arcsec between exposures. Data reduction was performed using the ORAC-DR pipeline which corrects the data for bias frames, bad-pixel masks, dark current subtraction and flat-field correction, and assembles the separate exposures into a final image. This is shown in Fig. 1 where B0128+437 can be seen as the relatively bright ($K = 17.8 \pm 0.3 \text{ mag}$) source in the centre. The source is resolved, despite the fact that the seeing ($\sim 0.5 \text{ arcsec}$) was approximately the same as the maximum image separation, with a peak to the north-west of the centre of the infrared detection. This is best seen in a contoured close-up view of B0128+437 that is also shown in Fig. 1. The shear galaxy is extremely faint in this image and can barely be seen above the noise.

It is tempting to associate the peak in the infrared image with the two merging images A and B as the majority of the radio emission is also located to the north-west of the centre of the system. This would suggest that the majority of the infrared emission is from the lensed source, but it is difficult to be sure of this due to the low resolution and the pointing accuracy of the UKIRT which is not sufficient to allow a direct comparison of the radio and infrared positions. We have improved on the original UKIRT astrometry by using the measured positions of four stars in the UKIRT field. Three of these stars have had positions measured using the Carlsberg Meridian Telescope (D. W. Evans, private communication) with the remaining star's position taken from the Two-Micron All-Sky Survey (2MASS). The addition of the 2MASS star is useful as it allows us to accurately calibrate the plate scale along both axes, the Carlsberg stars all lying in a narrow range of right ascension. The Carlsberg and 2MASS positions of a bright star in the field differ by only 10 mas showing that the two surveys are coincident. The astrometry calibration was performed using the Starlink GAIA program and places the UKIRT peak 100 mas to the west of images A and B, with a much smaller offset in declination. The total offset is approximately equal to the rms of the astrometric fit (80 mas) and thus we conclude that the UKIRT peak does correspond to the radio images A and B. The dominance of the lensed source in the infrared could stem from the presence of the redshifted [O III] doublet from the source in the passband.

3 VLBI OBSERVATIONS

Observations of B0128+437 were made at two separate epochs, the first at 5 GHz using the VLBA only (2000 December 20) and the second simultaneously at 2.3 and 8.4 GHz using the VLBA and the 100-m Effelsberg antenna (2002 January 2). On both occasions the source was observed for a total of $\sim 14 \text{ h}$, utilizing fast phase-referencing between the weak target and the nearby (37 arcmin distant) calibrator J0132+4325 with a cycling time of 4.5 min . Both epochs employed a data recording rate of 128 Mb s^{-1} with 2-bit sampling. This allowed, at 5 GHz , two contiguous 8-MHz bands (IFs) to be recorded, both with left (LCP) and right (RCP) circular polarizations. As the 2.3- and 8.4-GHz data were observed simultaneously, two contiguous 8-MHz bands were assigned to each frequency and only RCP was recorded. The data were subsequently processed using the VLBA correlator in Socorro, producing $16 \text{ } 0.5\text{-MHz}$ channels per IF and data averaged into 2-s bins. Cross-polarized visibilities were not produced as the MERLIN 5-GHz data show the images to be unpolarized.

The data were calibrated and mapped using the National Radio Astronomy Observatory (NRAO) AIPS software package. Once the flux scale was set using measurements of system temperature and a priori gain curves, phase slopes across the band were removed

using a short segment of data on a bright source. The phase-reference source was then fringe-fitted over the entire length of the experiment, solving for phase, phase rate and delay. The solutions so found were then transferred to the target. Secondary amplitude solutions were also derived from the phase calibrator. An additional step was undertaken at 2.3 GHz where the rapid phase variations caused by the ionosphere significantly degraded the success of the phase-referencing. We therefore used the AIPS task TECOR which attempts to remove the effects of the ionosphere using maps of the vertical total electron content (vTEC) of the atmosphere; these are produced by a network of global positioning system receivers. Application of the TECOR corrections significantly slowed the time variation of the phases of the phase-reference source and produced maps of B0128+437 with a higher dynamic range and with structures that were much more plausible given the prior knowledge we had from the 5-GHz data taken a year previously.

The data were then averaged in frequency from 16 channels per band to four and in time from 2-s into 10-s samples. In order to prevent the VLBA–Effelsberg baselines from dominating the final image, the visibility data weights were altered by taking their fourth root. Iterative mapping and self-calibration was then undertaken using the AIPS tasks IMAGR and CALIB, four maps being made at the location of each image as measured from the MERLIN 5-GHz map. At each frequency rms off-source noise levels were achieved that were close to the theoretical values.

4 VLBI MAPS

The final maps are shown in Figs 2–5 and reveal a wealth of image substructure. If we consider first only the 8.4-GHz maps, we see that images A, C and D all consist of three discrete and approximately colinear subcomponents. We have labelled these A1, A2, A3, etc., in Fig. 2. Correctly labelling each subcomponent within each image is made particularly easy due to the fact that one of the subcomponents (1) is much brighter than the others. This ensures that there is no ambiguity over which subcomponent in each image corresponds to the same part of the source. In contrast, image B looks significantly different to the other images and is in fact barely detected. There are, though, two distinct areas of emission (which we have highlighted with dashed circles in Fig. 2) which we identify with the lensed image despite their very low surface brightness ($\sim 3\sigma$). The circles in Fig. 2 are also reproduced in the 5- and 2.3-GHz maps.

At 5 GHz a very similar picture holds with images A, C and D still dominated by three compact components. This is seen most clearly in the maps of Fig. 3 where the use of uniform weighting (where the nominal visibility weights are modified by the local density of data points in Fourier space) emphasizes the longer baselines, thus producing the highest possible resolution. Image B is detected more securely here, although the image remains very weak. The emission that is detected lies within the western of the two circles that indicate the location of probable lensed emission at 8.4 GHz and appears to be concentrated in two small patches, separated by about 5 mas . There is no evidence of any emission within the easternmost circle. However, it is not only image B that is anomalous at this frequency as the relative brightnesses of the subcomponents in image C do not agree with those seen in images A and D. In these last two images, the central subcomponent (2) has a higher surface brightness than the other two, contrasting with the situation at 8.4 GHz where subcomponent 1 is the brightest. In image C, though, the central subcomponent has the lowest surface brightness. A final interesting feature of these maps is the obvious stretching of subcomponents A1 and A2 along the direction of the jet that is not seen in image D.

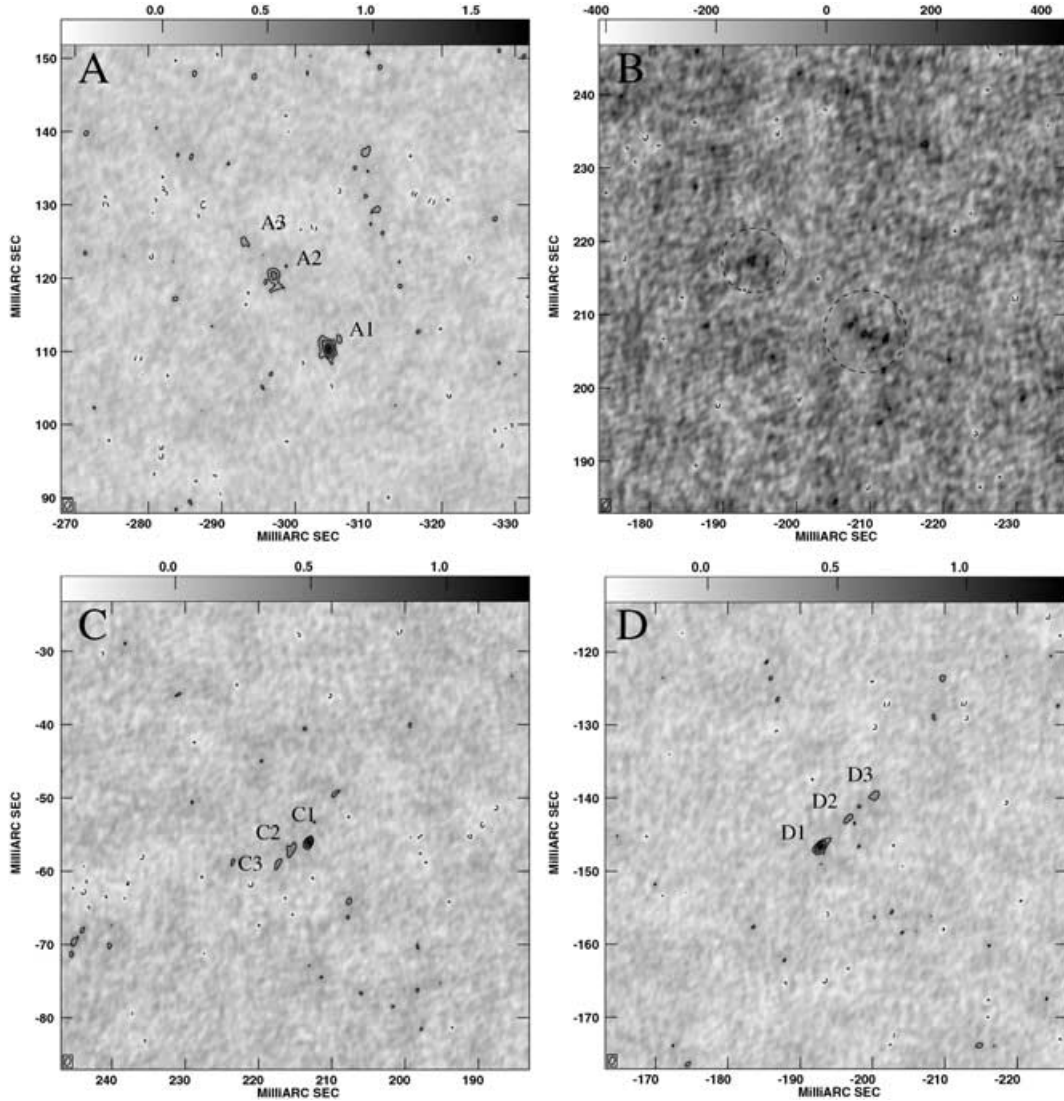


Figure 2. Naturally weighted VLBA + Effelsberg maps (RCP) of CLASS B0128+437 at 8.4 GHz. Contours are plotted at multiples ($-1, 1, 2, 4, 8$, etc.) of 3σ where σ is the off-source rms noise in the map ($90 \mu\text{Jy beam}^{-1}$). The restoring beam is shown in the bottom-left corner and has a FWHM of $1.2 \times 0.7 \text{ mas}^2$ at a position angle of $-21^\circ 6$. The grey-scales represent surface brightness in units of mJy beam^{-1} , apart from the map of image B where the units are $\mu\text{Jy beam}^{-1}$. Labels that identify the corresponding subcomponents in images A, C and D are plotted above. In the case of image B, we plot two dashed circles marking the location of what faint emission there is. The origin used for these and subsequent maps is $01^{\text{h}}31^{\text{m}}13^{\text{s}}.494, +43^\circ 58' 12''.805$ (J2000).

We have also made maps of the images at 5 GHz using natural weighting, i.e. without a correction for the density of visibility samples. These maps, shown in Fig. 4, are sensitive to larger-scale structures than those detected with uniform weighting and faint extended emission is detected in all images, e.g. along the jet axis in image A whilst C and D appear to sit in faint haloes. However, whilst these images appear similar to their uniformly weighted counterparts, image B looks dramatically different. Instead of the few weak patches of emission in the uniformly weighted map, this image is now detected with high signal-to-noise and is recognizable as an approximately straight jet with a length of $\sim 30 \text{ mas}$. The peak surface brightness lies at the south-western end of the jet which fades gradually towards the north-east.

We have fitted elliptical Gaussians to the 5-GHz visibility data using the OMFIT task in AIPS. We fitted nine Gaussians in total, one for each subcomponent in images A, C and D; image B is removed from the data by subtracting its CLEAN components found during

the naturally weighted deconvolution of the data. In calculating the errors it is assumed that the model is a perfect representation of the data, OMFIT scaling the weights attached to the visibility data (which are unknown in an absolute sense) until the χ^2 per degree of freedom ($\bar{\chi}^2$) of the model fit is equal to unity. As the images are dominated by compact emission we believe that this is a fairly safe assumption. The results of the model fit are shown in Table 1. Repeated trials, with different starting models, established that there is much more leeway in fitting parameters to image C than to the other images, presumably due to it being less well resolved. We therefore consider the model fits for image C to be less reliable than for the other images. Table 1 also shows the results of model fitting to subcomponents 1 only of the 8.4-GHz data, again using OMFIT. This demonstrates that subcomponents 2 and 3 have steeper spectra than 1 as this has a similar flux density at both frequencies whilst Figs 2–4 show that the other two significantly brighten. A comparison between the positions measured at 5 and 8.4 GHz indicate that

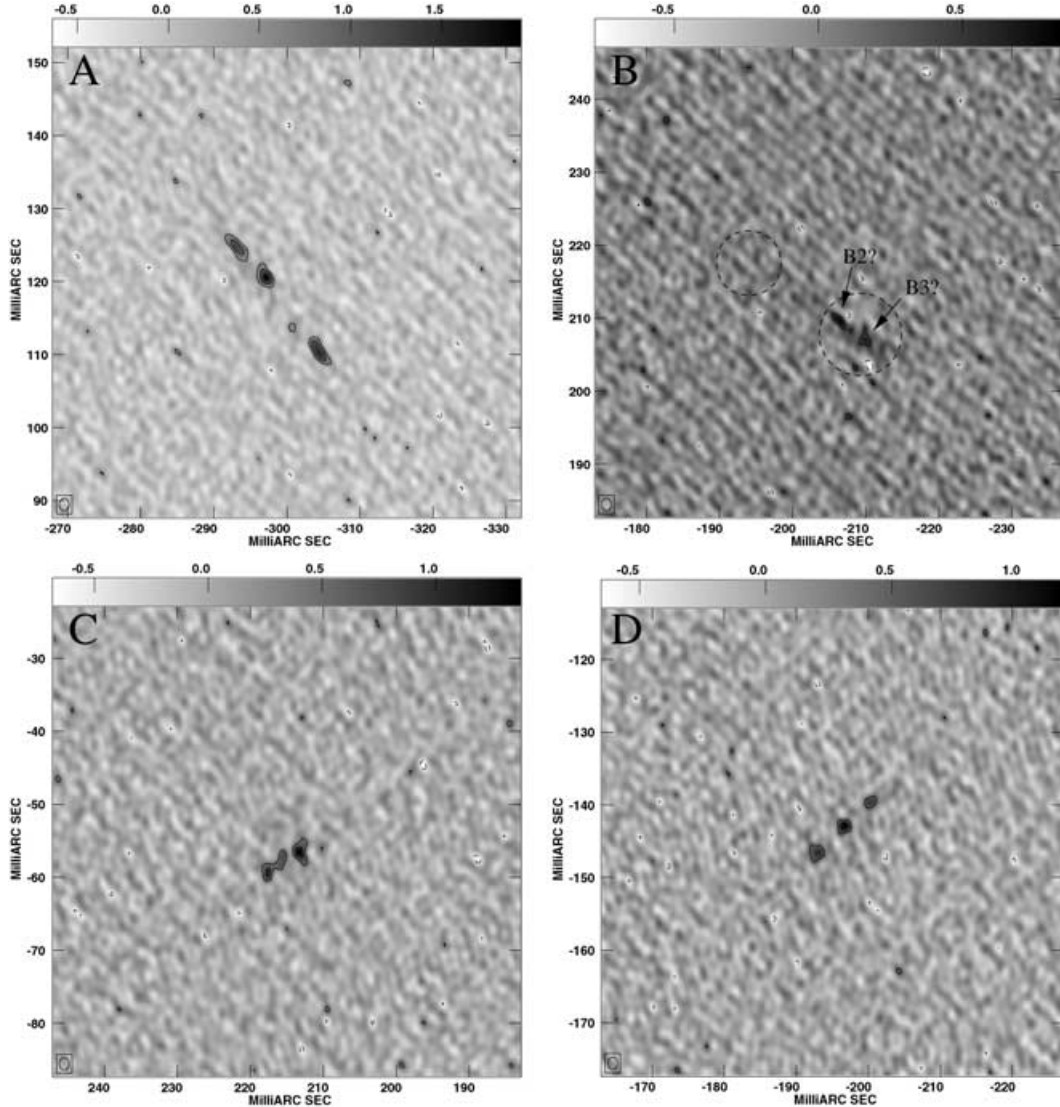


Figure 3. Uniformly weighted VLBA maps (Stokes I) of CLASS B0128+437 at 5 GHz. Contours are plotted at multiples ($-1, 1, 2, 4, 8$, etc.) of 3σ where σ is the off-source rms noise in the map ($155 \mu\text{Jy beam}^{-1}$). The restoring beam is shown in the bottom-left corner and has a FWHM of $1.7 \times 1.3 \text{ mas}^2$ at a position angle of $0^\circ.6$. The grey-scales represent surface brightness in units of mJy beam^{-1} . The maps are plotted on the same angular scale as the 8.4-GHz maps in Fig. 2. The same dashed circles that appear on the 8.4-GHz map of image B are reproduced here as a guide to the eye. We also label the possible identifications of subcomponents B2 and B3 (see Section 6.1).

the phase-referencing has been very successful, giving positions for subcomponent 1 that are the same to within 0.2 mas .

At the lowest frequency, 2.3 GHz, all the images look smoother and larger (Fig. 5) with little sign of the compact structures that dominate the images at the higher frequencies. This is due to a combination of the lower resolution and the increasing dominance of both the steep-spectrum subcomponents (2 and 3) and the surrounding extended jet emission at the lower frequency. There is, though, evidence that the subcomponents are being significantly resolved at 2.3 GHz as there is a lack of correlated flux on the longest baselines. This became apparent during phase self-calibration when practically no solutions could be found for Effelsberg, the most sensitive antenna in the array and the one contributing the longest baselines. This telescope was therefore flagged and does not contribute to the maps in Fig. 5; a map made using only the baselines to Effelsberg (sensitive to emission on scales of 3–4 mas) contains nothing but noise.

Finally, image B looks much more like image A at 2.3 GHz and it now becomes apparent that these images do point towards each other, as expected from lens models (see Section 5). However, inconsistencies between image B and image A remain, the most obvious being that the surface brightness of image B drops off very sharply about halfway along its length (at around $-200, 210 \text{ mas}$, between the two dashed circles) with the remaining half of the image barely detected. The correspondence in Fig. 5 between the contours and grey-scales, which represent the 5-GHz images, demonstrates that the phase-referencing has also been successful at 2.3 GHz, despite the problems introduced by the ionosphere.

5 LENS MODELLING

Our aim is to see if a lens model with a smooth mass distribution can fit the many new observational constraints now available. Phillips et al. (2000) were able to construct a model for the mass distribution

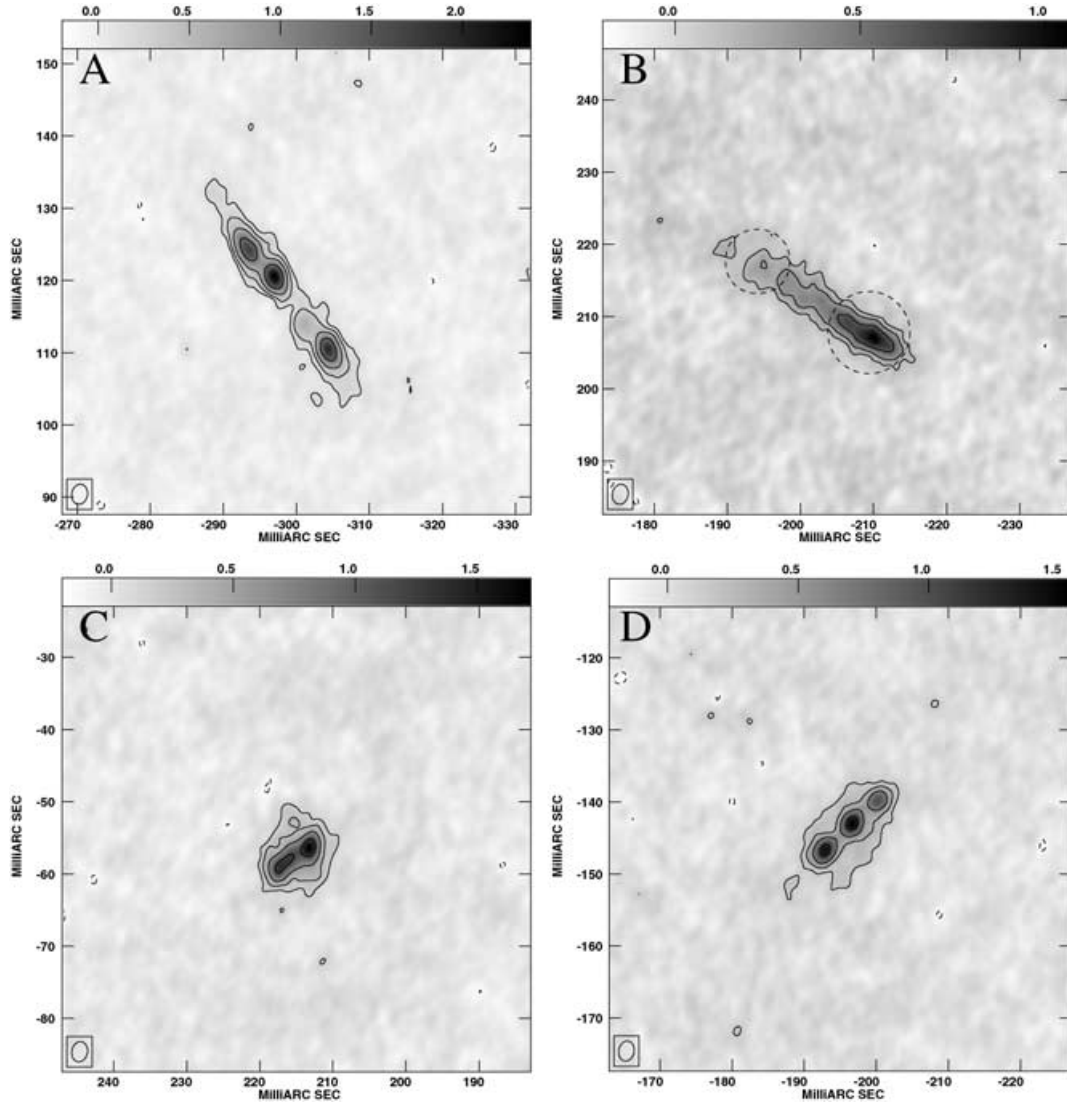


Figure 4. Naturally weighted VLBA maps (Stokes I) of CLASS B0128+437 at 5 GHz. Contours are plotted at multiples ($-1, 1, 2, 4, 8$, etc.) of 3σ where σ is the off-source rms noise in the map ($50 \mu\text{Jy beam}^{-1}$). The restoring beam is shown in the bottom-left corner and has a FWHM of $2.8 \times 2.2 \text{ mas}^2$ at a position angle of $-10^\circ.4$. The grey-scales represent surface brightness in units of mJy beam^{-1} . The maps are plotted on the same angular scale as the 8.4-GHz maps in Fig. 2. The same dashed circles that appear on the 8.4-GHz map of image B are reproduced here as a guide to the eye.

in the lens galaxy despite having no optical information regarding the position and light distribution in the galaxy. They found that a singular isothermal ellipsoid (SIE) model (e.g. Kormann, Schneider & Bartelmann 1994) including external shear was able to recover the MERLIN image positions and flux density ratios to within 1 mas and a few per cent, respectively. In this paper we attempt to improve the modelling by using the same parametrization, but incorporating the VLBI image constraints presented in Section 4. We have also experimented with the novel Fourier method of Evans & Witt (2003).

5.1 SIE + external shear parametrization

In order to be as rigorous as possible, we have performed the SIE modelling using three separate codes. Two of these are written by ourselves, IGLOO (NJJ) and GLINT (TY), as well as the LENSMODEL package (Keeton 2004). The results presented in this section all use full image-plane optimization for the greatest accuracy. We find that

the results of the modelling are broadly independent of the software used, although there are small differences. χ^2 , for example, can differ by up to a factor of a few and slightly different values for the galaxy parameters can be obtained, especially those that are degenerate. At no point do we use the flux densities to constrain the model as these may be affected by scattering in the lens galaxy (see Section 6.1). The models are still well constrained, though, due to the large number of degrees of freedom provided using the positional constraints alone.

Determining the image positions for image B is of course difficult due to the fact that the three subcomponents are not well defined in this image. We are forced therefore to use larger errors for this image. As inputs to the model we sometimes used the same position for all three subcomponents, a point close to the centre of the jet. On other occasions we used our best estimates of the positions of the B subcomponents from the VLBI maps (see, for example, Section 6.1). In both cases we assumed large (5–10 mas) errors on the positions.

Table 1. Flux densities, positions and shapes of the compact subcomponents identified in the VLBI observations, derived from the AIPS task OMFIT. The top half of the table gives the results for the three subcomponents of A, C and D derived from the 5-GHz data whilst the bottom half gives results for the 8.4-GHz data, for subcomponent 1 only. OMFIT was unable to determine values for parameters marked with a $-$. Position angles are measured north through east and positions are again offset from $01^{\text{h}}31^{\text{m}}13^{\text{s}}.494, +43^{\circ}58'12''.805$ (J2000).

Subcomponent	ν (GHz)	Flux density (mJy)	East offset (mas)	North offset (mas)	Major axis (mas)	Axial ratio	Position angle ($^{\circ}$)
A1	5	3.9 ± 0.1	-304.3 ± 0.1	110.4 ± 0.1	4.2 ± 0.2	0.27 ± 0.04	27.0 ± 2.1
A2	5	3.1 ± 0.2	-297.1 ± 0.0	120.6 ± 0.1	2.5 ± 0.2	0.20 ± 0.09	28.0 ± 2.9
A3	5	4.0 ± 0.2	-293.4 ± 0.1	124.4 ± 0.1	5.8 ± 0.4	0.16 ± 0.03	30.8 ± 1.5
C1	5	2.7 ± 0.1	213.2 ± 0.1	-56.3 ± 0.1	3.1 ± 0.2	0.42 ± 0.07	-10.1 ± 4.4
C2	5	1.2 ± 0.1	215.6 ± 0.1	-57.5 ± 0.1	1.9 ± 0.4	–	-9.2 ± 7.7
C3	5	1.6 ± 0.1	217.5 ± 0.1	-59.3 ± 0.1	2.0 ± 0.3	0.33 ± 0.14	-14.1 ± 7.2
D1	5	2.4 ± 0.1	-193.0 ± 0.1	-146.7 ± 0.1	3.5 ± 0.3	0.34 ± 0.06	-46.6 ± 3.9
D2	5	2.0 ± 0.1	-196.6 ± 0.1	-142.9 ± 0.1	1.7 ± 0.2	0.40 ± 0.14	-58.3 ± 8.5
D3	5	1.4 ± 0.1	-200.1 ± 0.1	-139.7 ± 0.1	2.0 ± 0.3	0.42 ± 0.18	-69.8 ± 11.4
A1	8.4	3.6 ± 0.3	-304.5 ± 0.1	110.4 ± 0.1	1.6 ± 0.2	0.31 ± 0.11	29.0 ± 6.5
C1	8.4	1.3 ± 0.2	213.1 ± 0.0	-56.1 ± 0.1	0.4 ± 0.3	–	-35.1 ± 37.3
D1	8.4	2.2 ± 0.2	-192.8 ± 0.1	-146.7 ± 0.1	1.1 ± 0.2	0.20 ± 0.22	-55.0 ± 8.0

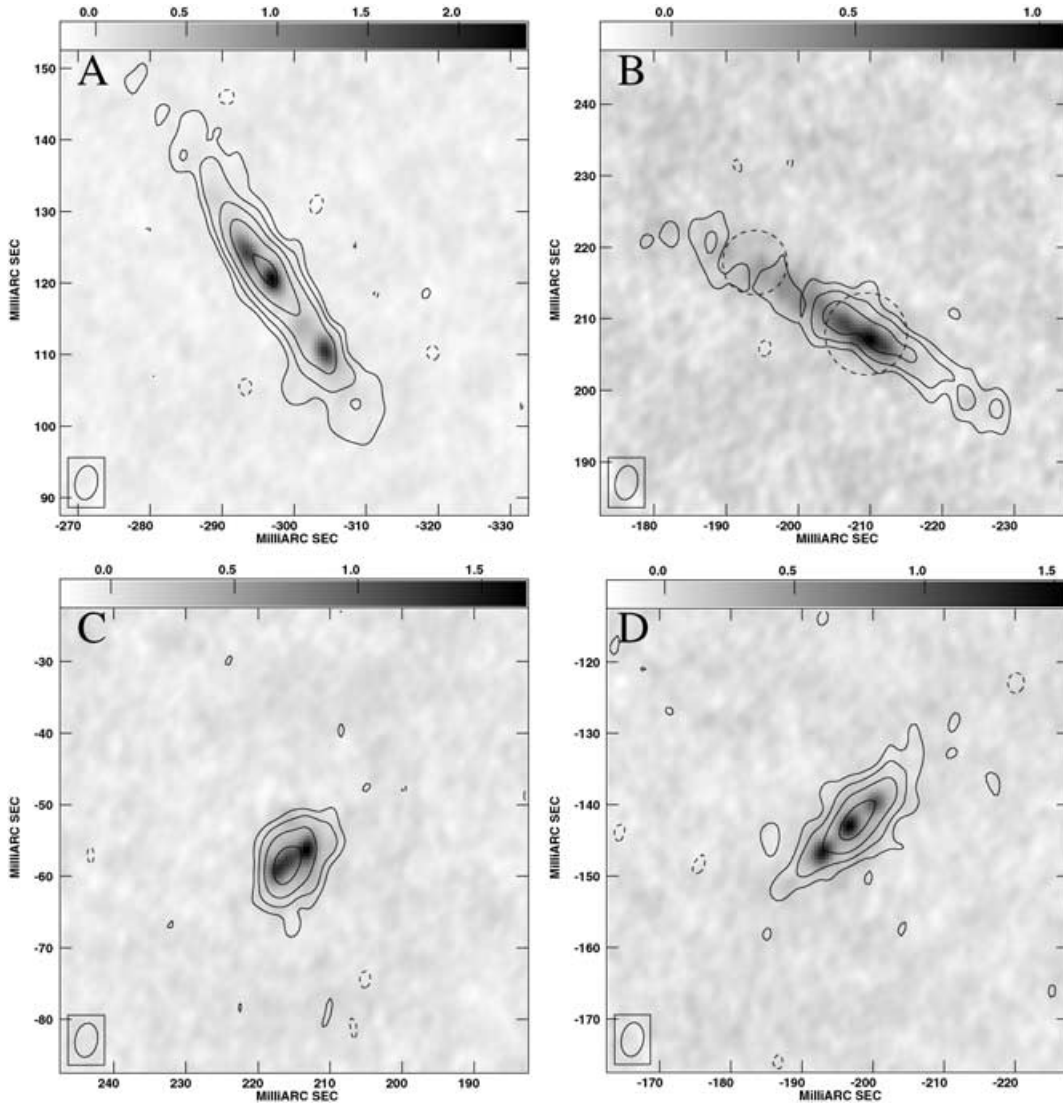


Figure 5. VLBA maps (RCP) of CLASS B0128+437 at 2.3 GHz (contours) made with a robust 0 weighting scheme. Contours are plotted at multiples ($-1, 1, 2, 4, 8$, etc.) of 3σ where σ is the off-source rms noise in the map ($100 \mu\text{Jy beam}^{-1}$). The restoring beam is shown in the bottom-left corner and has a FWHM of $4.8 \times 3.1 \text{ mas}^2$ at a position angle of $-10^{\circ}.1$. The grey-scaler shows the 5-GHz surface brightness distribution in units of mJy beam^{-1} . The maps are plotted on the same angular scale as the 8.4-GHz maps in Fig. 2 and the 5-GHz maps in Fig. 4. The same dashed circles that appear on the 8.4-GHz map of image B are again reproduced here.

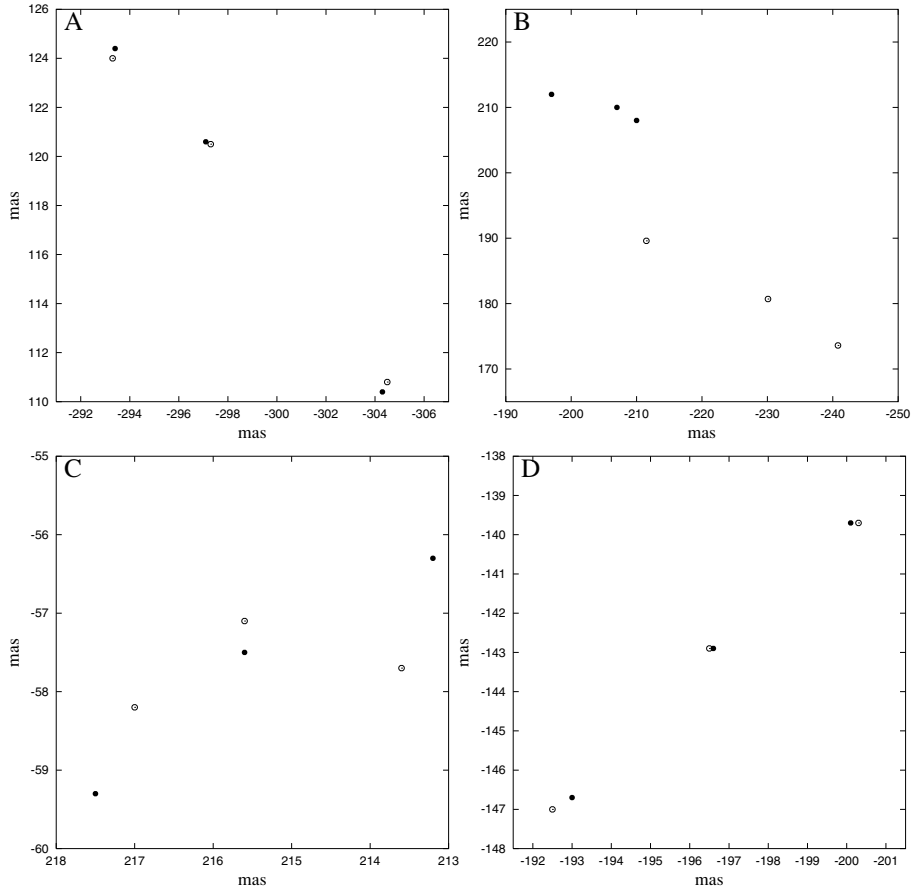


Figure 6. Observed positions of image subcomponents (filled circles) and derived model positions (open circles) for model 1 using the GLINT lens modelling software. The image B positional constraints have been estimated from the VLBI maps.

We begin by assuming that the true errors on the A, C and D subcomponent image positions are those found during the model fitting to the observational data, i.e. 0.1 mas. This we will refer to as model 1, with 5-mas errors assumed for the positions of the image B subcomponents. The fit found using model 1 is extremely poor, the χ^2 being equal to 635. With 11 degrees of freedom (24 positional constraints and 13 model parameters) this corresponds to a reduced χ^2 of 58. The reason for the high χ^2 can be seen in Fig. 6 where we plot the observed image positions along with those found after optimizing the model. Image B is fit very poorly (lying ~ 30 – 40 mas away from its observed position) as is image C, the modelled subcomponents C1 and C3 suffering from offsets of > 1 mas. The parameters of the optimized model are shown in Table 2.

Increasing the errors on images A, C and D by an order of magnitude to 1 mas (model 2) produces a better fit to image B and the expected improvement in the goodness-of-fit ($\chi^2 \sim 25$ and $\bar{\chi}^2 \sim 2$). The model positions are plotted in Fig. 7 and the lens galaxy parameters are again shown in Table 2. The model now places image B in the correct area of the image plane and the offsets between the observations and model lie between only 3 and 6 mas. These act to make the modelled jet too long, by about a factor of 2. The fit to image C, conversely, has deteriorated. The offsets of the end subcomponents have increased, to > 2 mas, thus accentuating a bend in the jet that was evident in Fig. 6. Images A and D again show no signs of any significant discrepancy.

These two models seem to highlight a degeneracy between the ability to fit either image B or image C, but not both. For example,

Table 2. Parameters for the SIE + external shear lens model. Listed are the galaxy Einstein radius (θ_E), position (x, y), magnitude and position angle of ellipticity ($\epsilon, \theta_\epsilon$) and magnitude and position angle of external shear (γ, θ_γ). Position angles are measured north through east and the galaxy position is offset from the VLBI phase centre (x increases to the east as with right ascension). For a description of the models see the text.

Parameter	Model 1	Model 2
θ_E	229 mas	237 mas
x, y	-81 mas, -4 mas	-79 mas, $+4$ mas
$\epsilon, \theta_\epsilon$	0.42, -51°	0.41, -36°
γ, θ_γ	0.26, 29°	0.22, 37°

we have also investigated the case when the image B positions are completely unconstrained in the model fit, i.e. their errors are made very large. In this latter case, we obtain $\chi^2 \sim 50$ which, with now only five degrees of freedom, gives a reduced χ^2 of ~ 10 . Excellent fits are found for images A and D, the observed positions being recovered to within the formal uncertainties. The modelled positions for image B, though, are highly discrepant, lying about 100 mas away from the observed position, a consequence of this image being completely unconstrained in the fit. Image C, though, is now fit relatively well, the offsets between modelled and observed positions being less than 0.5 mas for both C1 and C3.

Further simulations demonstrate the malleability of the model when various combinations of position errors are used as constraints.

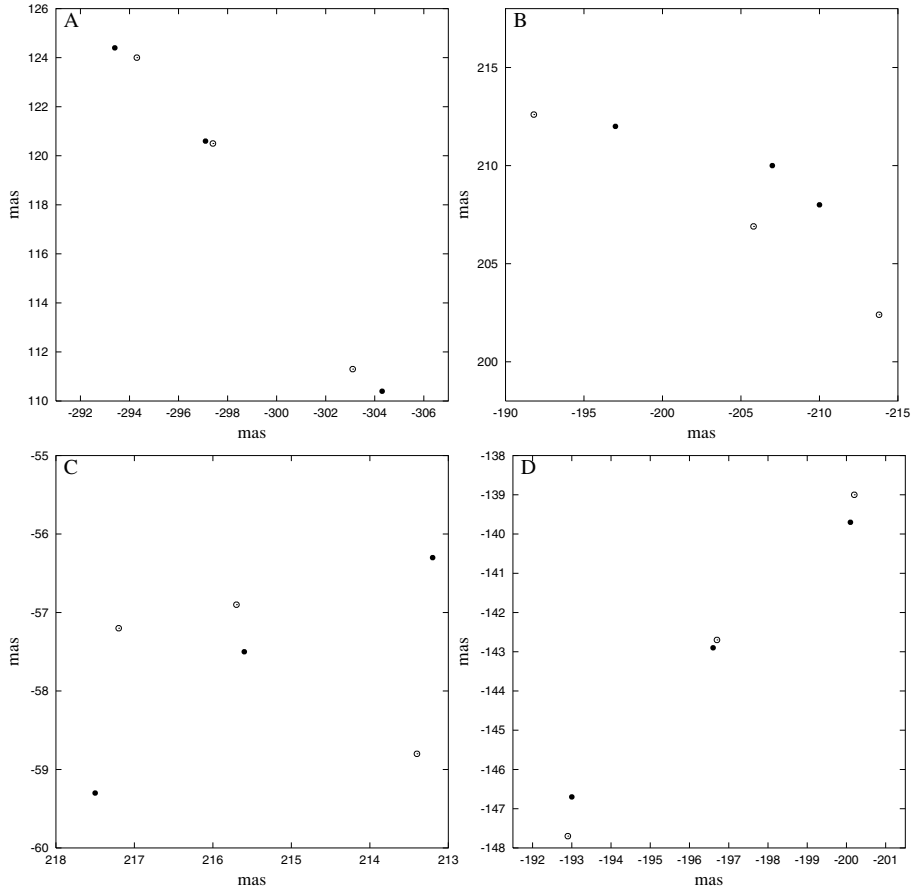


Figure 7. Observed positions of image subcomponents (filled circles) and derived model positions (open circles) for model 2 using the GLINT lens modelling software. The image B positional constraints have been estimated from the VLBI maps.

For example, we have found it possible to produce a progressively poorer fit to image A by reducing the errors on image C incrementally from 1 to 0.1 mas, whilst leaving the errors on A and D at 1 mas. This is accompanied by the ellipticity of the SIE increasing to ~ 0.9 . We also point out that the usual degeneracy between SIE ellipticity and external shear is present. This makes it very likely that different executions of a given modelling package (as well as different packages that use different optimization routines) will not converge to the same minimum.

However, the clear conclusion is that no smooth model can be obtained that fits all the astrometric constraints; it is not difficult to obtain a reasonable fit to images A and D but fitting both C and B simultaneously is not possible.

5.2 Evans & Witt method

Recently, Evans & Witt (2003) have introduced a method for lens modelling that models the lensing mass as a sum of Fourier components, the advantage of this being that the azimuthal profile is allowed to be completely arbitrary (whilst at the same time the galaxy is constrained to be isothermal and scale-free). This allows galaxies to be fit that are, for example, boxy or which contain bar-like structures. They have used their method to demonstrate that the anomalous flux ratios seen in some lens systems can, in some cases, be fit with a perfectly smooth galaxy, thus negating the need for CDM substructure to be invoked.

We have implemented our own version of the Evans & Witt method (with which we can reproduce the authors' results) and applied it to B0128+437. Initially we have only modelled a single source and find that it is relatively easy to fit a smooth galaxy, as should be expected given that the SIE + external shear model also works well in this case. However, when we increase the number of sources, first to two and then to three, we find it increasingly difficult to find a fit where the galaxy has smooth isophotes.

The optimization problem is, though, very complicated. The matrix that needs to be inverted (through singular-value decomposition) is very large for three sources (33×33) and, even with our use of a simulated annealing optimization algorithm, it is not clear how successful we are in locating the global minimum. An additional complication is that singular values which become very small need to be discarded. The choice of the threshold below which these are removed is crucial as this removes information and results in a smoother galaxy. For example, we find that a threshold of 10^{-5} of the largest singular value (with two sources modelled) produces similar results to a threshold of 10^{-4} (for three sources).

Bearing the above caveats in mind, we find results that are consistent with those found in the SIE + external shear modelling, using all three sources. With 1-mas errors on the image A, C and D subcomponents and 5-mas on B (EW1) we can produce a much smoother galaxy than we can using the nominal astrometric errors of 0.1 mas (EW2), for the same threshold (10^{-4}). In Fig. 8 we show the equidensity contours for these two models. The galaxy on the left (large errors) is clearly much smoother than that on the right which,

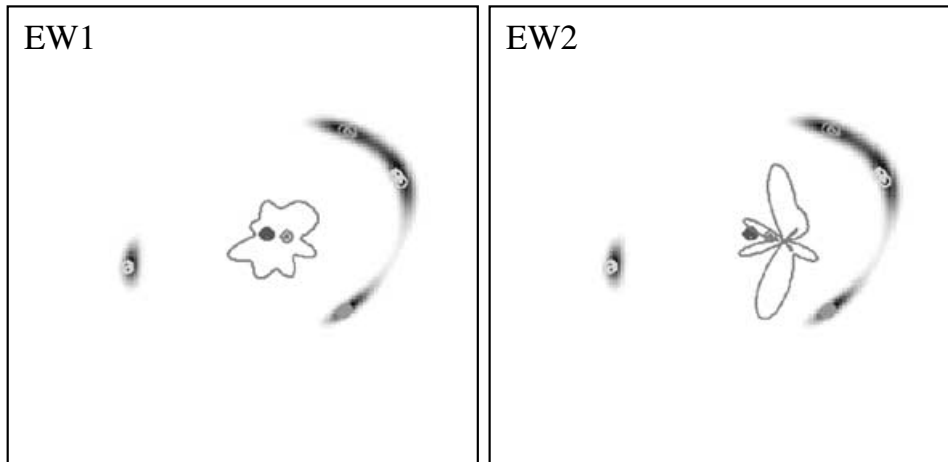


Figure 8. Results of applying the Evans & Witt method to all three sources of B0128+437. The model on the left (EW1) uses 1-mas errors on the A, C and D subcomponent positions whilst these are decreased to 0.1 mas in the model on the right (EW2). In both instances the errors on the image B positions are 5 mas and the singular-value threshold 10^{-4} . The thin grey lines represent equidensity contours of the lensing mass. The remainder of the plots shows the observed (circles) and modelled (grey-scales) image positions for an SIE + external shear model for scale. The circles close to the centre of the equidensity contours are the source and galaxy core (lighter of the two) positions.

in common with the SIE method, is consistent with the galaxy containing substructure.

6 DISCUSSION

Based on the initial work presented by Phillips et al. (2000) it appeared as though CLASS B0128+437 was a fairly ordinary lens system that could be simply and satisfactorily modelled. The observations and modelling presented here instead show that this system is problematic in at least two respects:

- (i) the strange appearance of image B, especially the absence of the subcomponents seen in the other images;
- (ii) the difficulty in fitting a mass model to the observed positions of the image subcomponents.

We now go on to discuss the origin of these as well as considering the flux ratios of the lensed images and the nature of the lensed source.

6.1 Scatter-broadening of image B

The most obvious and intriguing feature of the VLBI images of B0128+437 is that there is little sign in image B of the three discrete subcomponents that are so obvious in the other three images. However, examining the maps very carefully, it seems that B2 and B3 are in fact detected, albeit weakly. We identify these as the two weak patches of emission labelled in the uniformly weighted 5-GHz map of Fig. 3. This shows that the brightest end of the jet is actually made up of two discrete components separated by about ~ 5 mas, similar to the separation between subcomponents A2 and A3. Their location also places them at the correct end of the jet (the end nearest image A), the natural identification for the very faint emission seen at 8.4 GHz at the opposite end of the jet then being that this is probably the remnants of B1. We also note that the subcomponent that we identify as B2 has a higher surface brightness than B3, again in common with the equivalent subcomponents in A and D. The signal-to-noise is, however, low and the distortion of image B renders this identification far from definite.

However, what is causing image B to be so faint? The most likely explanation we believe is that this image is scatter-broadened in a

Table 3. The 5-GHz flux density of each image as measured from the VLBA maps, for both uniform and natural weighting.

	A	B	C	D
$S_{5,\text{uni}}$ (mJy)	10.6	2.8	4.8	4.8
$S_{5,\text{nat}}$ (mJy)	14.0	9.1	7.9	8.3
$S_{5,\text{uni/nat}}$ (mJy)	0.76	0.31	0.61	0.58

turbulent ionized medium. Contrary to the basic principles of gravitational lensing, surface brightness is clearly not conserved in image B, unlike in the other images (seen most clearly at 8.4 GHz). Scatter-broadening would naturally account for this as the flux contained within an image would be spread out over a larger area and thus appear fainter. The most convincing evidence for this effect in image B is its very different appearance in the uniform and natural maps, being very much stronger with natural weighting, whilst the other images look relatively similar under both weighting schemes. For example, whilst between 60 and 75 per cent of the naturally weighted total flux density is detected in the uniform maps of images A, C and D (as measured in an aperture around the image using the AIPS task TVSTAT) this drops to only 30 per cent for image B (Table 3). This indicates that the angular scale of image B is significantly larger than that of the other images, despite having a lower or comparable flux density. There is also no sign of the gap that exists approximately mid-way between A1 and A2 in image B.

A number of other features of image B support the scattering hypothesis. Our multifrequency maps show that the surface brightness of image B is not only lower than the other images, but that it has a different spatial and frequency dependence from the other images. At 5 GHz, the surface brightness of image B drops smoothly from its peak at the south-western area where B2 and B3 are located before fading away entirely around the location of B1. At 2.3 GHz, however, the reduction in surface brightness is much more pronounced, dropping very suddenly at around $-200, 210$ mas. It is clear from a comparison between Figs 4 and 5 that the area in between the

two dashed circles is brighter at 5 GHz than at 2.3 GHz, despite the surface brightness sensitivities of the two arrays being similar and the source being brighter at lower frequencies (above ~ 1 GHz). As scattering produced by a screen with uniform statistical properties over regions large in angular size compared to the source increases angular sizes proportional to the wavelength squared, the observed frequency dependence is in the correct sense. The spatial dependence is seen best at 8.4 GHz where similarly very weak emission is detected from all three subcomponents despite the fact that B1 should be much brighter.

If scatter-broadening is the explanation for the anomalous appearance of image B, there must be a cloud of clumpy ionized gas along the line of sight to image B and the strength of the scattering must increase towards the north-eastern end of the jet. The spatial dependence of the scattering within image B emphasizes the fact that the scattering within this lens system is non-uniform, i.e. image B alone is obviously affected. The most likely location of the scattering medium therefore is the lensing galaxy as this is the obvious location along a line of sight between the radio source host galaxy and our Galaxy where a large amount of ionized gas could reside and affect the images to different degrees. The small separation of the images predicts a relatively low mass for the lensing galaxy which may therefore be a spiral galaxy and rich in gas and dust. Other lens systems where images are believed to be scatter-broadened include PMN J0134–0931 (Winn et al. 2003a), JVAS B0218+357 (Biggs et al. 2003), PKS 1830–211 (Jones et al. 1996; Guirado et al. 1999) and CLASS B1933+503 (Marlow et al. 1999).

As a test for scattering elsewhere in B0128+437 we can examine the model fits to A1 and D1 for which we are able to measure sizes at two frequencies. We do not consider C1 as the small separation of the subcomponents in this image renders the model fits, especially their sizes, unreliable. Assuming that the angular size of the images (as measured by the geometrical mean of the major and minor axes, θ_g) scales as $\theta_g \propto \lambda^\alpha$, we measure $\alpha = 1.6 \pm 0.2$ for A1 and $\alpha = 2.5 \pm 0.4$ for D1. These increases are greater than the linear dependence on frequency usually expected for an optically thin synchrotron source and suggest that these images may also be affected by scattering. The haloes surrounding images C and D may also be a consequence of scatter-broadening as similar low surface brightness regions either side of the jet are not seen in the other images. We also note that although C2 is rather faint in Fig. 3 (uniformly weighted data), this is apparently not the case when natural weighting is used, i.e. this subcomponent, in common with image B, may be being scatter-broadened. However, the low resolution makes it difficult to be sure of this. (This flux ratio anomaly is also considered in the context of galaxy substructure in Section 6.2.)

We have considered other explanations for the anomalous appearance of image B, such as a lensing distortion due to compact structures within the lensing galaxy and free-free absorption, but these cannot explain all the effects observed in this image including its larger size relative to the other images as well its frequency-dependent reduction in surface brightness.

6.2 Lens substructure

The SIE lens modelling that we have undertaken has demonstrated that it is not possible to reproduce the observed model positions of the VLBI subcomponents in B0128+437 unless we assume that the nominal error bars on the subcomponent positions are large underestimates of the true uncertainties. Using the nominal errors produces a poor fit to the data, the most striking aspect of this being that image B is offset by tens of mas from its observed position.

While there is of course some uncertainty in the positions of the image B subcomponents, it is certainly not greater than 5 mas, and less if our identification of B2 and B3 in Fig. 3 is correct. The fact that we have used error bars on the image B positions which are 50 times larger than those on the other images explains why this image is so poorly constrained during the optimization.

Most striking about the model is the degeneracy we find between the model's ability to fit the positions of B and C. The best fit for image C is found when image B is completely unconstrained (its modelled position ending up very close to that of image A) whilst the better the agreement with the observed position of image B, the poorer the fit to image C. Given that we must insist that the model produces positions for image B that are consistent with the observations to at least several mas, the coupling we find between the positions of images B and C means that we must accept that the model cannot reproduce the positions of the subcomponents in image C.

As we cannot fit the observed image positions with a smooth parametrization of the mass in the lensing galaxy (a conclusion which is also suggested by the results of the Evans & Witt method) then there must be additional unmodelled mass in the deflector, i.e. substructure. Hierarchical models of large-scale structure formation such as CDM predict that galactic haloes should contain a population of satellites with masses that extend down to at least $10^7 M_\odot$, the current resolution of the best simulations (e.g. Moore et al. 1999; De Lucia et al. 2004). Our own galaxy contains an order of magnitude less satellites than predicted and many authors have recently considered gravitational lensing as a way of implying the presence of these objects in lensing galaxies, mainly through the detection of anomalous flux ratios (e.g. Dalal & Kochanek 2002; Metcalf & Zhao 2002), but also through image position shifts and distortions (e.g. Wambsganss & Paczyński 1992; Metcalf & Madau 2001; Metcalf 2002).

We believe that the need to increase the uncertainties on the subcomponent positions (by a factor of 10) to 1 mas in order to gain an acceptable fit is evidence that some form of substructure is present in the lens galaxy of B0128+437. The modelled position shifts of several mas imply substructure of at least $\sim 10^6 M_\odot$. If a perturbing mass was located close to image C, this could also affect the flux ratios of the image C subcomponents, perhaps explaining why the central subcomponent, C2, is so faint in Fig. 3 (but see Section 6.1 for an alternative hypothesis).

Conclusions based on the lens mass modelling should be strengthened with improved optical/infrared images of the lens system with which the properties of the lensing mass (positions, shape, etc.) could be measured and used as model constraints. This may be possible with approved *HST* NICMOS observations that should take place in 2004.

6.3 Flux density ratios

The radio data do not allow the production of spectra for each image across a very wide range of frequencies. The only data that cleanly separate each image, other than those obtained with VLBI, are the MERLIN 5-GHz data although MERLIN at 1.4 GHz and the Very Large Array (VLA) at 8.4 GHz do resolve images C and D. We consider the flux densities measured from the VLBI data to be less accurate than those from the VLA and MERLIN data, but the 2.3-GHz image shown in Fig. 1 [where the images are nearly at their brightest and where a (u, v) taper has been applied thus increasing the sensitivity to low surface brightness emission] should be fairly reliable.

Table 4. Flux density ratios for various image combinations at four frequencies (X, 8.4 GHz; C, 5 GHz; S, 2.3 GHz; L, 1.4 GHz).

	VLA (X)	MERLIN (C)	VLBA (S)	MERLIN (L)
$S_{B/A}$	–	0.56	0.49	–
$S_{C/A}$	–	0.49	0.34	–
$S_{D/A}$	–	0.47	0.47	–
$S_{C/D}$	0.67	1.04	0.72	0.75

We have estimated flux densities at each frequency by model fitting to the visibilities, except at 2.3 GHz. In this case we use a variety of methods including summing the CLEAN components, measuring the flux contained within an aperture as well as summing all pixels that have a surface brightness greater than 6σ of the rms map noise. All methods gave broadly consistent results and we have taken their average as the best estimator at this frequency. We only consider the flux ratios, as these are not subject to errors in the absolute flux density scale, and we show these in Table 4.

Given $\lesssim 5$ per cent errors on the flux density ratios, the most surprising thing about the numbers in Table 4 is the flux density of image C relative to image D. At three of the four frequencies (1.4, 2.3 and 8.4 GHz) C is significantly fainter than D whilst at 5 GHz the flux densities of each are the same to within the errors. The 5-GHz data would not appear to be in error as the same flux density ratios were measured from 41 epochs of data that were observed as part of a project to look for radio microlensing in a sample of JVAS/CLASS lens systems (Koopmans et al. 2003; Biggs et al., in preparation). Similarly, the fact that a ratio of ~ 0.7 is measured at the other three frequencies strongly argues that these measurements are also robust and that the flux ratio anomaly is real. The MERLIN monitoring data also showed that the flux density of each image was constant over the eight-month monitoring period, which rules out intrinsic source variability as the cause and demonstrates that the effect is long-lived. Interpretation of this effect would be greatly aided by additional observations that would allow the flux density of each image to be measured accurately over a range of frequencies. This could be done with the VLA at 15 and 22 GHz, in conjunction with the VLBA Pie Town antenna at 8.4 and 5 GHz.

6.4 Lensed radio source

The radio source in B0128+437 is a member of the GPS class as its spectrum peaks at around 1 GHz. This allowed Phillips et al. (2000) to estimate the maximum angular separation that would be observed in VLBI observations based on a correlation of this between the turnover frequency and the source flux density (Snellen et al. 2000). Our observations confirm their prediction of substantial resolved structure in this system.

We are also able to measure the spectral indices of the individual subcomponents between 5 and 8.4 GHz. This is done most easily for subcomponent 1, the only particularly bright one in each image at 8.4 GHz, where we measure $\alpha \sim -0.16$ for A1 and D1, where $S_\nu \propto \nu^\alpha$. Model fitting to the 8.4-GHz (u, v) data gives a flux density for A2, the brightest subcomponent 2 image, of ~ 1.6 mJy which corresponds to a much steeper spectrum of $\alpha \sim -1.27$. The third subcomponent also has a steep spectrum, but this is difficult to measure due to its weakness in all images at 8.4 GHz.

The fact that one of the outer subcomponents has a flat spectrum suggests that this is the core and that the source is a classical core-jet. However, at 5 GHz (the only frequency where reliable sizes can

be measured for all three subcomponents) the most compact subcomponent is the central one. Furthermore, emission is detected on either side of the flat-spectrum subcomponent at both 5 and 2.3 GHz. Both of these observations are unusual as it is more commonly the flat-spectrum core component that is the most compact and core-jet sources, which are believed to point more or less towards the observer, should not display counterjet emission as this should be greatly reduced in brightness due to Doppler de-boosting.

Also unusual is the presence of low-brightness extended emission in the 2.3-GHz maps. This would not be expected given that the source spectrum peaks at 1 GHz (the total flux density at 325 MHz is only ~ 15 mJy; Phillips et al. 2000). B0128+437 is, in this respect, similar to another lens system, JVAS B2114+022, where two of the components (which may or may not be lensed) are very diffuse, despite having spectra that turn over above 1 GHz (Augusto et al. 2001). It may be that the turnover in the spectrum is not intrinsic to the source, but a consequence of a propagation effect such as free-free absorption. Another possibility is that the spectrum is intrinsic and that the low-brightness extended emission results from scatter-broadening, as has already been suggested for image B.

7 SUMMARY AND CONCLUSIONS

We have presented VLBI observations of the gravitational lens system CLASS B0128+437 that reveal extensive structure within each of the four images. These data illustrate the role that high-resolution VLBI observations play in the study of lens systems, such as providing a large number of model constraints and identifying inconsistencies between the observations and the lens model. Interesting astrophysical conclusions regarding the lens galaxy can be drawn that would otherwise be missed using data from smaller arrays such as MERLIN and the VLA. Our observations demonstrate that despite the large number of model constraints made available by the VLBI imaging, we find it difficult to obtain smooth mass models to fit the observed image positions, signifying additional unmodelled structure in the deflector. This may be another instance of lensing providing evidence to support the existence of mass substructure in CDM haloes. Improved infrared *HST* observations will be taken which may improve our understanding of the deflecting mass, leading to more rigorous modelling.

The most striking feature of our new VLBI maps is the anomalous appearance of image B compared to the other images. The most likely explanation for this is that this image is being scatter-broadened in the interstellar medium of the lensing galaxy, a process which may also be affecting the other images to a lesser extent. An important consequence of this effect concerns the identification of lens systems in CLASS. The CLASS methodology was to use VLBA 5-GHz observations, once candidate systems had been identified with the VLA and MERLIN, to see whether any could be rejected on the basis of surface brightness arguments, i.e. weaker components more extended, or through inconsistent structures in the different images. In a two-image system particularly, were one of the images to be distorted in a manner similar to that seen in B0128+437, that system may have been rejected. We are currently re-observing 13 CLASS two-image lens candidates at 15 GHz with the VLBA in order to check whether their initial rejection was sound.

7 ACKNOWLEDGMENTS

MAN, JPM, PMP and TY acknowledge the receipt of Particle Physics and Astronomy Research Council (PPARC) studentships.

The VLBA is operated by the NRAO, which is a facility of the National Science Foundation (NSF) operated under cooperative agreement by Associated Universities, Inc. This work included observations with the 100-m telescope of the Max-Planck-Institut für Radioastronomie (MPIfR) at Effelsberg. This work also included observations made with the National Aeronautics and Space Administration/European Space Agency (NASA/ESA) *HST*, obtained at the Space Telescope Science Institute, which is operated by AURA, Inc., under NASA contract NAS 5-26555. The UKIRT is operated by the Joint Astronomy Centre on behalf of PPARC. This publication makes use of data products from the 2MASS, which is a joint project of the University of Massachusetts and the Infrared Processing and Analysis Centre/California Institute of Technology, funded by NASA and the NSF. We thank the referee, David Rusin, for his comments.

REFERENCES

- Augusto P. et al., 2001, *MNRAS*, 326, 1007
 Biggs A. D., Wucknitz O., Porcas R. W., Browne I. W. A., Jackson N. J., Mao S., Wilkinson P. N., 2003, *MNRAS*, 338, 599
 Bradač M., Schneider P., Steinmetz M., Lombardi M., King L. J., Porcas R., 2002, *A&A*, 388, 373
 Browne I. W. A. et al., 2003, *MNRAS*, 341, 13
 Burud I. et al., 2002, *A&A*, 391, 481
 Chae K. H. et al., 2002, *Phys. Rev. Lett.*, 89, 151301
 Dalal N., Kochanek C. S., 2002, *ApJ*, 572, 25
 De Lucia G., Kauffmann G., Springel V., White S. D. M., Lanzoni B., Stoehr F., Tormen G., Yoshida N., 2004, *MNRAS*, 348, 333
 Evans N. W., Witt H. J., 2003, *MNRAS*, 345, 1351
 Fassnacht C. D., Xanthopoulos E., Koopmans L. V. E., Rusin D., 2002, *ApJ*, 581, 823
 Guirado J. C., Jones D. L., Lara L., Marcaide J. M., Preston R. A., Rao A. P., Sherwood W. A., 1999, *A&A*, 346, 392
 Helbig P., Marlow D., Quast R., Wilkinson P. N., Browne I. W. A., Koopmans L. V. E., 1999, *A&AS*, 136, 297
 Jones D. L. et al., 1996, *ApJ*, 470, L23
 Keeton C. R., 2004, *ApJ*, submitted (astro-ph/0102340)
 Kochanek C. S., 2003, *ApJ*, 583, 49
 Kochanek C. S. et al., 2000, *ApJ*, 543, 131
 Koopmans L. V. E., Treu T., 2003, *ApJ*, 583, 606
 Koopmans L. V. E. et al., 2003, *ApJ*, 595, 712
 Kormann R., Schneider P., Bartelmann M., 1994, *A&A*, 284, 285
 Lehár J. et al., 2000, *ApJ*, 536, 584
 McKean J. P., Koopmans L. V. E., Browne I. W. A., Fassnacht C. D., Blandford R. D., Lubin L. M., Readhead A. C. S., 2004, *MNRAS*, in press
 Mao S., Schneider P., 1998, *MNRAS*, 295, 587
 Marlow D. R., Browne I. W. A., Jackson N., Wilkinson P. N., 1999, *MNRAS*, 305, 15
 Metcalf R. B., 2002, *ApJ*, 580, 696
 Metcalf R. B., Madau P., 2001, *ApJ*, 563, 9
 Metcalf R. B., Zhao H., 2002, *ApJ*, 567, L5
 Moore B., Ghigna S., Governato F., Lake G., Quinn T., Stadel J., Tozzi P., 1999, *ApJ*, 524, L19
 Muñoz J. A., Kochanek C. S., Keeton C. R., 2001, *ApJ*, 558, 657
 Myers S. T. et al., 2003, *MNRAS*, 341, 1
 Phillips P. M. et al., 2000, *MNRAS*, 319, L7
 Refsdal S., 1964, *MNRAS*, 128, 307
 Rusin D., Ma C., 2001, *ApJ*, 549, L33
 Rusin D., Norbury M., Biggs A. D., Marlow D. R., Jackson N. J., Browne I. W. A., Wilkinson P. N., Myers S. T., 2002, *MNRAS*, 330, 205
 Snellen I. A. G., Schilizzi R. T., Miley G. K., de Bruyn A. G., Bremer M. N., Röttgering H. J. A., 2000, *MNRAS*, 319, 445
 Treu T., Koopmans L. V. E., 2002, *MNRAS*, 337, L6
 Wambsgans J., Paczyński B., 1992, *ApJ*, 397, L1
 Winn J. N., Kochanek C. S., Keeton C. R., Lovell J. E. J., 2003a, *ApJ*, 590, 26
 Winn J. N., Rusin D., Kochanek C. S., 2003b, *ApJ*, 587, 80

This paper has been typeset from a $\text{\TeX}/\text{\LaTeX}$ file prepared by the author.